Carbon 99 (2016) 591–598

Contents lists available at ScienceDirect

Carbon

journal homepage: www.elsevier.com/locate/carbon

Metal-free chemical vapor deposition growth of graphitic tubular structures on engineered perovskite oxide substrates

Jingyu Sun [1], Frank Dillon, Chen Wu [2], Jun Jiang, Kerstin Jurkschat, Antal A. Koós [3], Alison Crossley, Nicole Grobert**, Martin R. Castell*

University of Oxford, Department of Materials, Parks Road, Oxford, OX1 3PH, UK

ARTICLE INFO

Article history:
Received 10 November 2015
Received in revised form
14 December 2015
Accepted 26 December 2015
Available online 29 December 2015

ABSTRACT

Metal-free growth of carbon nanotubes/fibers (CNT/Fs) using chemical vapor deposition (CVD) on semiconducting and insulating substrates is of interest in the context of the construction of nanoscale electronic devices. However, controllable synthesis of CNT/Fs without the aid of metal catalysts is an ongoing challenge. Here we report the direct CVD synthesis of CNT/Fs on the perovskite oxides $SrTiO_3$ (STO) and $Ba_{0.6}Sr_{0.4}TiO_3$ (BST). A variety of processing steps were used on STO (001) substrates to create a set of six patterns with varying atomic-scale surface roughnesses. These substrates were all subjected to the same CVD growth conditions, and a correlation was found between the surface roughness of the substrates and the density of CNT/Fs. This indicates that nanometer-scale asperities on the substrates act as the catalytically active sites for CNT/F growth. In a separate set of experiments the surfaces of polished polycrystalline BST samples were investigated. The random orientation of the exposed etched facets of the individual grains revealed significantly different catalytic activity for CNT/F growth. Our study demonstrates the great influence of the nature of the crystal surface condition on the catalytic activity of the substrates and is a critical first step towards perovskite oxide catalyst design.

1. Introduction

Many evolving electronic technologies require low dimensional carbon materials such as graphene and carbon nanotubes or fibers (CNT/Fs) that are free from the residues of metal catalysts. Metal-catalyst-free growth of novel carbon nanomaterials has been achieved to date by using chemical vapor deposition (CVD) processes in conjunction with oxides and nitrides as the catalysts materials [1–7]. For example, graphitic layers have been grown on MgO crystals [8], graphene has been synthesized on SiO_2 [9–13], Al_2O_3 [14,15] and glass [16–18] surfaces, and single-walled CNTs have been generated from SiO_2 [19–21] and TiO_2 [22,23] particles/composites.

Perovskite oxides, such as $SrTiO_3$ (STO) and $BaSrTiO_3$ (BST), are important technological materials that are used as oxygen sensors [24], as electrodes in fuel cells [25], in tunable microwave systems [26], and as catalysis platforms [27,28]. Recently we reported that a BST substrate was able to accommodate the controlled growth of carbon helical structures [27] and a further study by Sun et al. demonstrated that high-quality monolayer graphene can be grown directly onto STO single crystals via catalyst-free CVD [29].

In this paper we present the results of a series of experiments where CVD was used to synthesize CNT/Fs on the perovskite oxides STO and BST. The main result is that variations in the nanometer-scale surface structure give rise to differences in CNT/F yields that vary by orders of magnitude. This insight will be a cornerstone in the design of future perovskite oxide catalyst materials for the growth of graphitic tubular structures.

2. Experimental

2.1. STO (001) substrate engineering

Epi-polished STO (001) samples (PI-KEM Ltd, UK), doped with

* Corresponding author.
** Corresponding author.
E-mail addresses: nicole.grobert@materials.ox.ac.uk (N. Grobert), martin.castell@materials.ox.ac.uk (M.R. Castell).
[1] Current address: Cambridge Graphene Centre, University of Cambridge, 9 JJ Thomson Avenue, Cambridge CB3 0FA, United Kingdom.
[2] Current address: School of Materials Science and Engineering, Zhejiang University, Hangzhou 310027, China.
[3] Current address: Centre for Energy Research, Institute of Technical Physics and Materials Science, Budapest 1121, Hungary.

http://dx.doi.org/10.1016/j.carbon.2015.12.084
0008-6223/

0.5%wt Nb were used as substrates. An ultra-high vacuum (UHV) system, incorporating a treatment chamber, an Ar^+ ion sputter source, and a scanning tunneling microscope (STM) [24], was used for the treatment and characterization of the substrates prior to their transfer to the CVD growth apparatus. A series of STO (001) substrates with different surfaces structures was created as reported in detail in our previous papers [30–38]. Below we briefly summarise the preparation conditions.

Sputtered: The as-received STO sample was first degassed, followed by Ar^+ ion bombardment with an ion energy of 0.75 keV and an ion flux of 1.28 A m^{-2} for 20 min. This procedure leads to the roughest surface that was investigated.
BHF-etched: The as-received STO sample was etched for 10 min in a buffered HF (NH_4F–HF) solution (pH = 4.5), in accordance with the recipe described by Kawasaki et al. [39] This treatment removes any surface SrO layers resulting in a rough surface with only TiO_2 terminations.
Degassed: The as-received STO sample was introduced into the UHV system and annealed at 600 °C for up to 1 h. This process produces a relatively rough surface, but where most of the surface contamination has been removed.
(2×1)-reconstructed: This reconstructed surface was prepared by annealing the sample in UHV at 800 °C for 30 min.
Nanostructured: The surface decorated with TiO_2 nanostructures was produced by Ar^+ ion sputtering (0.75 keV, 1 A m^{-2}, 10 min) and subsequently annealing in UHV at 900 °C for 30 min.
c(4×2)-reconstructed: The STO (001) c(4 × 2) reconstructed surface was produced through Ar^+ ion sputtering (0.75 keV, 1 A m^{-2}, 10 min), followed by annealing at 1200 °C for 15 min.
Scratched: To create the scratched STO substrates, as-received STO samples were first etched in the BHF solution for 5 min and then scratched using a diamond scribe to avoid any metal contamination. This procedure results in STO particles deposited around the scratch site (Fig. S1, Supporting Information).

2.2. Polycrystalline BST substrate engineering

Epi-polished polycrystalline $Ba_{0.6}Sr_{0.4}TiO_3$ substrates (PI-KEM Ltd, UK) were used. The BST samples were etched for 10 min in the BHF solution, as described above, and then cleaned using ethanol and deionized water.

2.3. CVD procedure for the growth of CNT/Fs

For CNT/F growth, both EtOH-CVD and C_2H_2-CVD were carried out on the STO and BST substrates. The substrates were inserted into a quartz tube (2.2 cm inner diameter), which was then placed in a 50 cm long horizontal furnace. To ensure that the process was completely free of metal catalysts, a brand new quartz furnace tube was employed for each CVD run, and plastic tools were used for sample handling. For EtOH-CVD, C_2H_5OH (Aldrich 99.5%) was used as the carbon feedstock and was introduced via an ultrasonic piezo-driven aerosol generator (RBI Pyrosol 7901). In a typical CVD experiment, C_2H_5OH was carried by an Ar/H_2 mixture and introduced to the furnace tube after it had reached the growth temperature. After the growth, the furnace was switched off and the quartz tube was cooled down to room temperature in Ar. For C_2H_2-CVD, C_2H_2 (BOC, UK) as carbon feedstock was directly introduced along with Ar and H_2, the gas flow rate was always set at 20–40 standard cubic centimetres per minute (sccm) for the duration of growth. It is worth noting that the samples were subjected to an H_2 (800 sccm for 5 min) anneal at the growth temperature before the introduction of the carbon feedstock (C_2H_5OH or C_2H_2).

2.4. Characterization

Prior to the CVD growth process, the set of STO (001) substrates was characterized with an STM (JEOL JSTM 4500xt) using an electrochemically etched W tip with the bias voltage applied to the sample. The polycrystalline BST substrates were characterized using an atomic force microscope (AFM) (Veeco Park CP AutoProbe) operated in tapping mode. Following the growth of the CNT/Fs, the samples were analyzed in a JEOL JSM 840F scanning electron microscope (SEM, 5 kV), and a JEOL JEM 4000HR transmission electron microscope (TEM, 80 kV). The quality of the CNT/Fs was determined by Raman spectroscopy using a JY Horiba Labram Aramis imaging confocal Raman microscope with a 532 nm frequency doubled Nd:YAG laser. Electron backscatter diffraction (EBSD) measurements were performed in a JEOL JSM 6500F SEM at 20 kV. White-light interferometric microscopy (Micro-XAM) data were generated with an Omniscan Micro-XAM 5000B 3D instrument. Elemental analysis for the grown samples was performed using energy-dispersive X-ray spectroscopy (EDX) in an SEM (JEOL JSM 840A) and a TEM (JEOL JEM 2010) TEM. X-ray photoelectron spectrometry (XPS) was performed with radiation from the Mg Kα band (hυ = 1253 eV) using a VG Clam electron energy spectrometer.

3. Results and discussion

3.1. Surface-roughness-tailored growth of CNT/Fs on STO (001) substrates

Surface roughness studies were conducted by preparing a series of substrates that all exhibited different surface structures. These were as follows: Ar^+ ion sputtered, BHF-etched, degassed, (2 × 1)-reconstructed, nanostructured and c(4 × 2)-reconstructed. The preparation processes are described in the experimental section. Fig. 1 shows typical STM images of the c(4 × 2) (a_1), nanostructured (b_1) and sputtered (c_1) surfaces in the left column and the corresponding representative SEM images following CNT/F growth in the right column (a_2-c_2). The same growth conditions for all the samples was EtOH-CVD in an Ar/H_2 (400/200 sccm) atmosphere at a growth temperature of 700 °C for 30 min. The different surface structures clearly give rise to different yields of CNT/Fs. The atomically flat c(4 × 2) reconstructed surface yields no measurable CNT/Fs and appears to be catalytically inert, whereas the Ar^+ ion sputtered sample produces a dense matt of CNT/Fs.

We carried out a detailed investigation of the Ar^+ ion sputtered sample, before and after CNT/F growth. The SEM, transmission electron microscopy TEM, and Raman spectroscopy results are shown in Fig. S2. The CNT/Fs had typical diameters between 8 and 18 nm, an areal density of $3.4 \times 10^9 \pm 1.7 \times 10^9$ cm^{-2}, and were of good quality considering the relatively low growth temperature of 700 °C. To verify that a metal-catalyst-free growth process had indeed taken place, XPS measurements were performed on the sputtered samples before and after CVD growth (Fig. S3), and no metal contaminants were found.

To investigate the relationship between the roughness of the surfaces and their CNT/F yield, we carried out a detailed analysis of the samples with different surface structures. In addition to the images from Fig. 1, the STM images of the BHF-etched, degassed, and (2 × 1)-reconstructed samples are shown next to their CNT/F growths in Fig. S4. The areal root-mean-square (rms) surface roughness of the various STO substrate surfaces and the corresponding areal CNT/F count is plotted in Fig. 2. The rms surface roughness for each substrate was obtained by typically averaging the results of 20 STM images. The values of the densities of CNT/Fs were obtained by analyzing the SEM micrographs. The errors (shown as error bars along both the x and y axes in the plot)

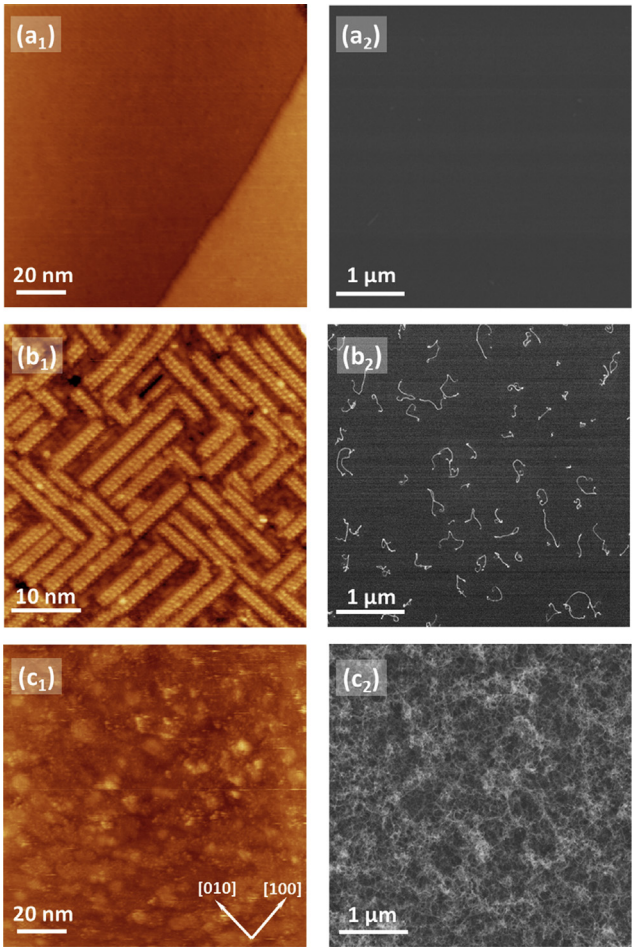

Fig. 1. Surface structure dependent CNT/F growth on $SrTiO_3$ (001) substrates by direct EtOH-CVD. Left column: STM images of (a_1) c(4 × 2)-reconstructed, (b_1) nanostructured, and (c_1) sputtered substrates. Right column: (a_2-c_2) SEM images of CNT/Fs grown on corresponding $SrTiO_3$ substrates. (A color version of this figure can be viewed online).

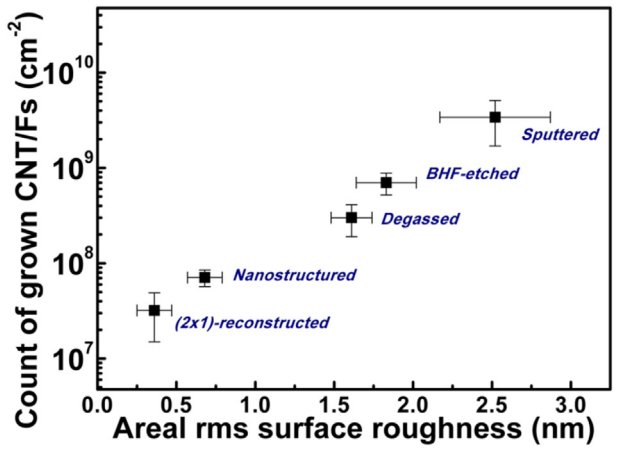

Fig. 2. Plot of the areal rms surface roughness of the $SrTiO_3$ (001) substrates versus the areal density of CNT/Fs grown on them by CVD. (A color version of this figure can be viewed online).

represent the standard deviations of the measurements. The data point for the c(4 × 2)-reconstructed surface (rms roughness 0.15 ± 0.07 nm) is not included in the plot because no CNT/Fs were seen on this surface after the CVD process. It should also be pointed out that there was a significant variation in the yield obtained from the (2 × 1)-reconstructed samples, where some of these surfaces showed a very low CNT/F yield. In Fig. 2 the (2 × 1) data point is only made up from (2 × 1) surfaces where a meaningful measurable yield was observed.

As can be readily seen in the plot, there is a strong correlation between the rms roughness of the surfaces of the samples and the logarithm of the CNT/F density. This relationship leads us to speculate that nanoscale STO surface asperities act as the nucleation sites for CNT/F growth. Highly ordered surfaces, such as the atomically flat c(4 × 2) and (2 × 1) reconstructed surfaces have very few asperities that are large enough to stimulate CNT/F growth. In contrast, the Ar^+ ion sputtered surface has a broad range of asperities of varying sizes and shapes that can readily act as CNT/F nucleation sites.

Early work on laser-etched quartz substrates also suggested that surface roughness may play a significant role in the nucleation behavior of multi-wall carbon nanotubes [40]. To further investigate the nature of STO asperities for stimulating CNT/F growth, we carried out EtOH- and C_2H_2-CVD on STO scratched substrates. Scratching the STO surface prior to CVD using a diamond scribe leads to the generation of a surface containing nanometer- and micron-sized STO particles with a variety of curvatures. For EtOH-CVD, our growth experiment was carried out at a temperature of 700 °C. The samples were subsequently characterized by SEM, EDX, XPS and Raman spectroscopy, and indicate that CNT/Fs were generated from the scratching mark via a metal-catalyst-free process (Fig. S5). The results from the C_2H_2-CVD growth at 700 °C are shown in Fig. 3. The SEM micrograph in Fig. 3a shows the CNT/Fs that grew on the scratched sample. The TEM image in Fig. 3b shows that the formation of CNT/Fs occurs at the periphery of the white-circled particle marked with a "c". EDX measurements from the catalyst particle "c" are presented in Fig. 3c and show the presence of the elements Sr, Ti, O, C, and Cu, which result from the $SrTiO_3$ catalyst particle, the carbon CNT/F, and the copper TEM grid (Fig. 3d). XPS measurements were also performed on the samples (Fig. 3e), and there is no indication of the presence of conventional types of metal catalysts (e.g. Fe, Co, Ni). This study of the scratched surface complements the previous results on the set of STO (001) surfaces and provides further evidence that STO asperities and small particles act as catalysts for the nucleation of CNT/Fs during CVD growth.

3.2. *Facet-orientation-dictated growth of CNT/Fs on BST polycrystal substrates*

So far we have shown how an STO crystal with the (001) crystallographic orientation can be modified in different ways to produce surfaces that have different CNT/F yields. In the next part of the paper we show that the facet orientation of individual grains within a BST polycrystal is also a significant factor in catalyzing the nucleation and growth of CNT/Fs. The BST polycrystals were delivered pre-polished and prior to carrying out our experiments we etched them in a BHF solution. The etching treatment removes the polishing damage and any metal nanoparticle contamination, giving rise to a clean polycrystalline BST surface with a large variety of randomly oriented grain facets. These samples were characterized by SEM, AFM and Micro-XAM as shown in Fig. S6, which show typical grain diameters of the order of a few μm. To grow CNT/Fs on the etched BST samples, EtOH-CVD and C_2H_2-CVD were employed at a growth temperature of 750 °C with mixed carrier gases (Ar/H_2: 500/500 sccm) flowing during the reaction. EDX and XPS analyses for the etched and post-grown samples were performed to verify that a metal-catalyst-free CVD process had taken place (Fig. S7).

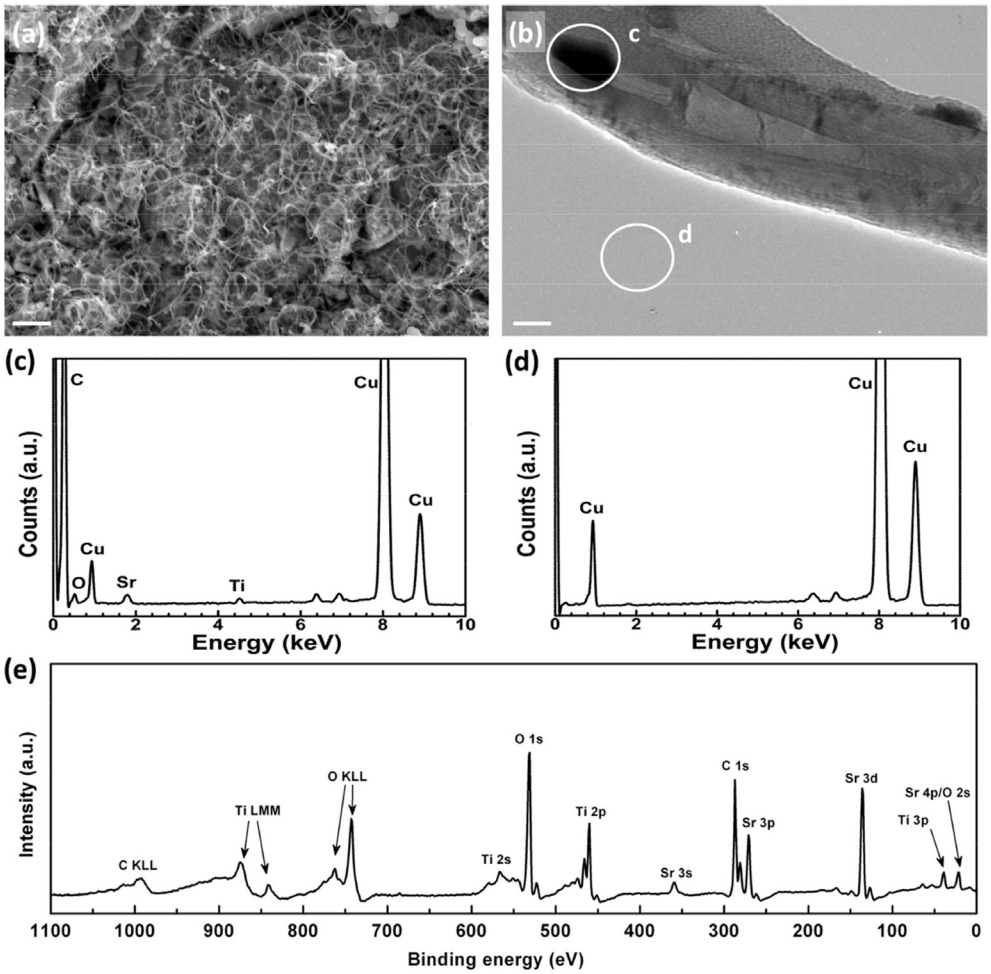

Fig. 3. Characterization of CNT/Fs grown on scratched $SrTiO_3$ surfaces by C_2H_2-CVD at a growth temperature of 700 °C. (a) SEM and (b) TEM observations of the grown sample. Scale bars: (a) 500 nm. (b) 20 nm. (c,d) EDX spectra of the white-circled regions in (b). The EDX spectrum (c) of the catalytic nanoparticle trapped within the tube demonstrates that it is $SrTiO_3$. The EDX spectrum (d) of the TEM grid shows the Cu background signal. (e) XPS spectrum of the as-grown sample showing a surface that is free from metallic species such as Fe, Co, Ni and Cu.

The influence of the facet orientation of the grains on the CNT/F yield can be clearly seen in the SEM image library shown in Fig. 4. Some facets support prolific growth of CNT/Fs, whereas other facets produce nothing at all. Fig. 4a and b are SEM images at different magnifications, which show the growth of CNT/Fs on the BST polycrystalline surface by EtOH-CVD. Similar growth behavior was observed when C_2H_2-CVD was used (Fig. 4c and d). Shorter growth times of 30 s were also tested (Fig. 4e and f) and show ostensibly the same result, namely that the CNT/Fs nucleation sites vary considerably depending on the grain facets. The influence of grain orientations has been investigated in detail by us with respect to the CVD growth of graphene on Cu foil [41]. The quality of the as-grown CNT/Fs was evaluated by Raman spectroscopy. The representative Raman spectrum of the sample (Fig. 5) displays the three characteristic peaks of graphitic tubular structures at the D (~1350 cm^{-1}), G (~1580 cm^{-1}) and 2D bands (~2690 cm^{-1}), confirming the high purity of samples prepared in this work. It is worth-mentioning that the Raman spectrum of a carbon nanotube displays a 2D peak similar to that of graphene, which is not too surprising as it is regarded as a rolled up sheet of graphene. The 2D band is the second order of the D band, which is due to double resonance, linking the phonon wavevectors to the electronic band structure [42]. The importance of Raman 2D band for carbon nanomaterials lies in the fact that it can be efficiently used to monitor the number of layers for graphene [43] as well as to distinguish the doping type of carbon nanotube [44].

The intensity of G band relative to that of the D band (I_G/I_D) is often used as a measure of the quality with nanotubes, where a comparison between obtained and published results is meaningful to characterize the sample quality. The calculated I_G/I_D ratio in Fig. 5 is ~1.2, indicating that the carbon nanostructures are indeed CNT/Fs but contain many defects. Representative results on the growth of CNT/Fs over non-metallic catalysts are summarized in Table 1, with the highlight of Raman I_G/I_D ratio. Note that our growth were normally carried out at low reaction temperatures (*i.e.* <800 °C) during metal-free CVD processes, the conditions of which are consistent with the results reported in Refs. [46,47]. Our future work would aim at the enhancement of CNT growth quality by increasing the reaction temperature and/or designing perovskite oxide catalyst nanoparticles.

To further probe the phenomenon of facet-related growth behavior, SEM, electron backscatter diffraction (EBSD) and Micro-XAM were used to co-investigate the same regions of the sample following CNT/F growth. Fig. 6a–c depict an area of interest, where the center of the images represent the same triple-junction. The SEM image in Fig. 6a displays facet-selective growth of CNT/Fs on the three grain facets. The facets numbered 1 and 3 contain a substantial number of CNT/Fs, whereas facet 2 does not support

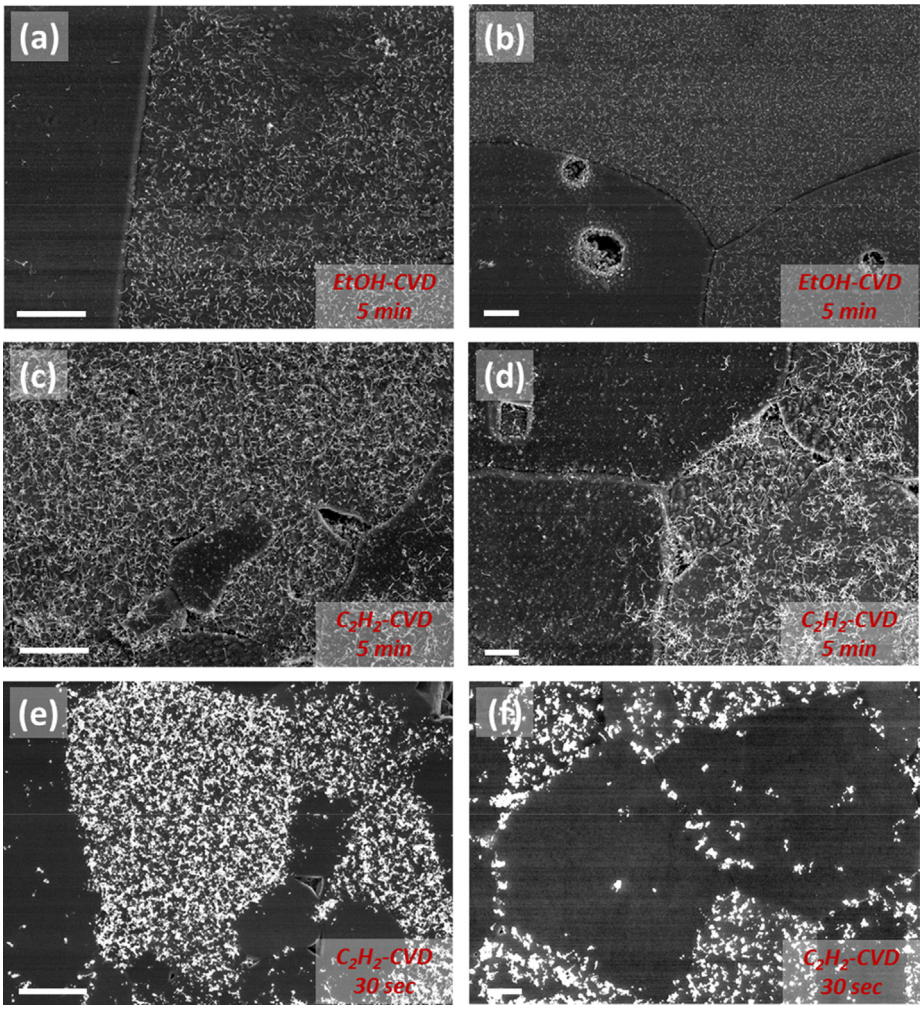

Fig. 4. SEM image library of facet-selective growth of CNT/Fs grown on polycrystalline BHF-etched $Ba_{0.6}Sr_{0.4}TiO_3$ surfaces. (a,b) EtOH-CVD and (c,d) C_2H_2-CVD were conducted for growth periods of 5 min (e,f) Running C_2H_2-CVD for 30 s allows the observation of the nucleation stage of CNT formation. Scale bars: (a), (c) and (e) 3 μm. (b), (d) and (f) 1 μm. (A color version of this figure can be viewed online).

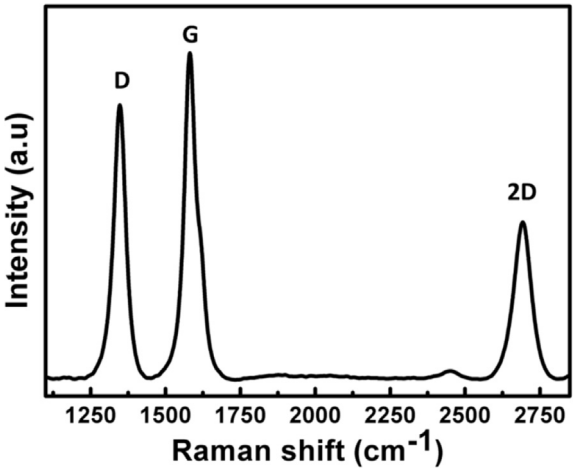

Fig. 5. Representative Raman spectrum of CNT/Fs grown on BHF-etched $Ba_{0.6}Sr_{0.4}TiO_3$ polycrystalline substrates.

CNT/F growth. Facet 1 has a greater areal density of CNT/Fs of $(41.5 \pm 0.7) \times 10^8$ cm^{-2} compared with facet 2 $[(23.8 \pm 0.9) \times 10^8$ $cm^{-2}]$. Fig. 6b shows the EBSD map of the three

Table 1
Comparison of our work and previous reports on the growth of CNT/Fs by means of metal-free CVD routes.

Substrate	Obtained CNT/F type	Raman I_G/I_D	Ref.
SiO_2/Si	Single-walled CNTs	25	[20]
Diamond	Single-walled CNTs	5–12	[45]
Carbon black	Multi-walled CNT/Fs	0.7–1.1	[46]
Glass	Multi-walled CNT/Fs	0.9–1.1	[47]
STO, BST	Single/Multi-walled CNT/Fs	1.2	This work

different facets, which have substantially different orientations. Facets 1, 2, and 3 lie near the (110), (001) and (111) crystal planes, respectively, as shown in the colored EBSD triangle. The grains in the polycrystalline sample are randomly oriented so we expect random facet exposure on the sample surface. It is therefore simply good fortune that we were able to select a triple junction in Fig. 6 that displays three facets that are close to the main crystallographic directions. The Micro-XAM image taken from the same area is shown in Fig. 6c, which shows small height differences between the grains. These height differences are likely to indicate that the BHF etching solution stripped away material to different depths. It was not possible to use STM or AFM to measure the rms roughnesses of the different facets because of the irregular nature of the

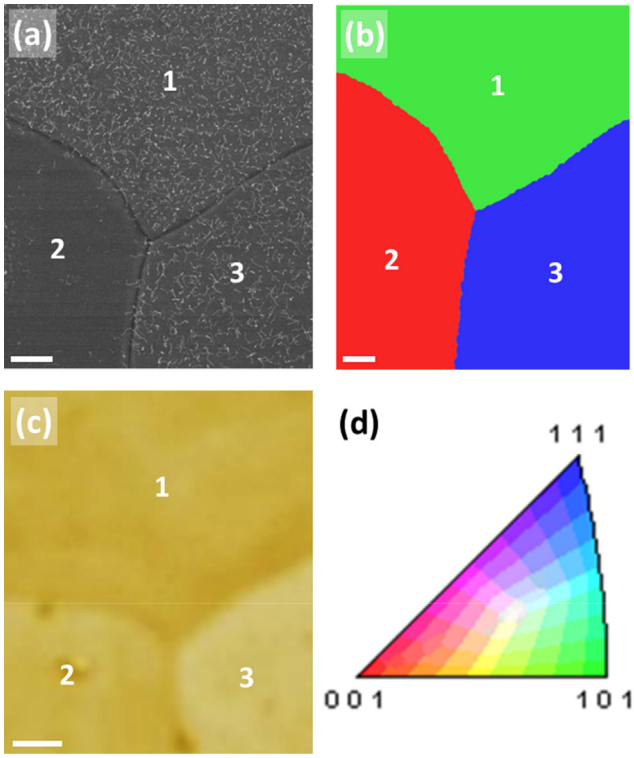

Fig. 6. (a) SEM, (b) EBSD and (c) Micro-XAM co-investigation of facet-selective growth of CNT/Fs on a BHF-etched $Ba_{0.6}Sr_{0.4}TiO_3$ polycrystalline surface. The images were taken from the same triple-junction on the sample. The numbers marked on each image indicate the three different grain facets. A color triangle, used to index the EBSD map in (b), is also shown in (d). Scale bars: (a) 1 μm. (b) 5 μm. (c) 2 μm. (A color version of this figure can be viewed online).

polycrystalline surface that included pinholes. However, it is reasonable to assume that the different facets respond differently to the BHF etching process, resulting in different roughnesses on the grain surfaces. As shown earlier for the STO (001) sample as well as in other studies [19,48], surface roughness is one of the paramount factors for producing CNT/Fs within a catalyst-free process. The (001) surface is generally the most stable in perovskite oxides, and will therefore likely to result in a smooth surface following the BHF etch. It is therefore not surprising that facet 2 in Fig. 6, which lies near the (001) orientation has the lowest CNT/F yield.

Fig. 7 shows a further set of results from SEM, EBSD and Micro-XAM co-investigations of three different areas on the sample. The CNT/F growth on the facets marked by yellow-colored numbers in Fig. 7a_1-c_1 are shown in the high-magnification SEM images in Fig. 7a_2-c_2. The EBSD maps are shown in Fig. 7a_3-c_3 and the Micro-XAM images in Fig. 7a_4-c_4. Qualitative investigation of the data in Fig. 7 indicates that facets that are near the (001) orientation (red in a_3-c_3) have the lowest CNT/F yield. Specifically these facets are numbers 2 and 4 in (a_3) and facet 3 in (b_3). In contrast, facets near the (110) orientation (green in in a_3-c_3) have relatively high CNT/F yields. This finding is in agreement with the results of Fig. 6. The Micro-XAM images in Fig. 7 serve to demonstrate the different etching rates on the grains. For example, in (a_4) grain 2 is 96 ± 27 nm higher than neighboring grain 4. We do not have a sufficiently exhaustive data set to attempt a quantitative analysis of the data in Fig. 7, but feel that there is enough evidence to speculate that the BHF etch results in different surface roughnesses on the different facets and that this is responsible for the varying CNT/F yields. Further, the facets near the stable (001) orientation ought to be the smoothest and therefore have the lowest yields.

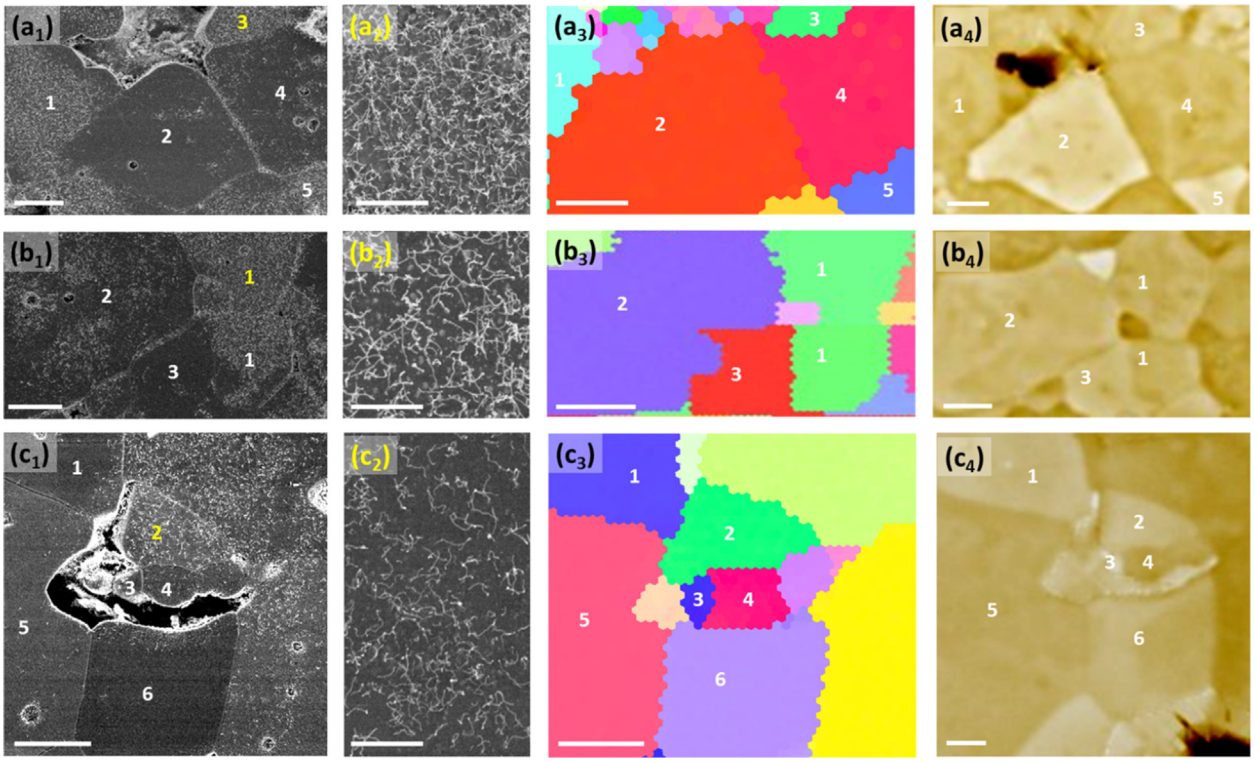

Fig. 7. (a_1-c_1) SEM overviews of three different areas of the $Ba_{0.6}Sr_{0.4}TiO_3$ polycrystal following CNT/F growth. (a_2-c_2) High magnification SEM of the CNT/Fs. (a_3-c_3) EBSD and (a_4-c_4) Micro-XAM co-investigations of facet-selective growth of CNT/Fs with each row corresponding to the same site of interest. The numbers marked on the images indicate the different crystal facets for each position. The CNT/F growth on the facets marked by yellow-colored numbers are correspondingly shown in the high-magnified SEM images in (a_2-c_2). Scale bars: (a_1-c_1) 5 μm. (a_2-c_2) 1 μm. (a_3-c_3) 5 μm. (a_4-c_4) 10 μm. (A color version of this figure can be viewed online).

4. Conclusions

In summary we have demonstrated that perovskite oxides can serve as effective catalysts to initiate the growth of CNT/Fs by a direct CVD route. Based on this observation, we developed a series of approaches to engineer the surfaces of STO (001) single crystals to achieve roughness-tailored growth of CNT/Fs. We also demonstrated facet-orientation-selective growth of CNT/Fs on BST polycrystalline substrates, and speculate that the surface roughness due to the BHF etching process is similarly the key element in determining CNT/F yield. This work shows that the nanoscale surface roughness of perovskite oxides is central to controlling the catalytic reactivity and hence the yield for CNT/F growth. This result is a milestone in the understanding of the design of future non-metal catalysts for CNT/F synthesis.

Acknowledgments

We are grateful to the Royal Society (NG), European Community's Sixth and Seventh Framework Programme [DEDIGROWTH (ERC-2009-StG-240500); CONTACT (Marie-Curie-ITN-238263), BNC Tubes (FP6-NMP-033350)] (NG) and Chinese Ministry of Education-University of Oxford Scholarship (JS) for financial support. We also thank Chris Spencer (JEOL, UK) for valuable STM technical support and Xiao Hu (Oxford Materials, UK) for EDX data processing.

Appendix A. Supplementary data

Supplementary data related to this article can be found at http://dx.doi.org/10.1016/j.carbon.2015.12.084.

References

[1] A. Nel, T. Xia, L. Madler, N. Li, Toxic potential of materials at the nanolevel, Science 311 (5761) (2006) 622–627.
[2] M.H. Rümmeli, C. Kramberger, A. Gruneis, P. Ayala, T. Gemming, B. Buchner, et al., On the graphitization nature of oxides for the formation of carbon nanostructures, Chem. Mater. 19 (17) (2007) 4105–4107.
[3] G. Hong, Y. Chen, P. Li, J. Zhang, Controlling the growth of single-walled carbon nanotubes on surfaces using metal and non-metal catalysts, Carbon 50 (6) (2012) 2067–2082.
[4] K.S. Novoselov, V.I. Fal'ko, L. Colombo, P.R. Gellert, M.G. Schwab, K. Kim, A roadmap for graphene, Nature 490 (7419) (2012) 192–200.
[5] D. Jariwala, V.K. Sangwan, L.J. Lauhon, T.J. Marks, M.C. Hersam, Carbon nanomaterials for electronics, optoelectronics, photovoltaics, and sensing, Chem. Soc. Rev. 42 (7) (2013) 2824–2860.
[6] L.L. Tan, W.J. Ong, S.P. Chai, A.R. Mohamed, Growth of carbon nanotubes over non-metallic based catalysts: a review on the recent developments, Catal. Today 217 (2013) 1–12.
[7] J. Sun, Y. Zhang, Z. Liu, Direct chemical vapor deposition growth of graphene on insulating substrates, ChemNanoMat (2016), http://dx.doi.org/10.1002/cnma.201500160.
[8] M.H. Rümmeli, A. Bachmatiuk, A. Scott, F. Borrnert, J.H. Warner, V. Hoffman, et al., Direct low-temperature nanographene CVD synthesis over a dielectric insulator, ACS Nano 4 (7) (2010) 4206–4210.
[9] J. Chen, Y. Wen, Y. Guo, B. Wu, L. Huang, Y. Xue, et al., Oxygen-aided synthesis of polycrystalline graphene on silicon dioxide substrates, J. Am. Chem. Soc. 133 (44) (2011) 17548–17551.
[10] H. Bi, S. Sun, F. Huang, X. Xie, M. Jiang, Direct growth of few-layer graphene films on SiO_2 substrates and their photovoltaic applications, J. Mater. Chem. 22 (2) (2012) 411–416.
[11] J. Chen, Y. Guo, L. Jiang, Z. Xu, L. Huang, Y. Xue, et al., Near-equilibrium chemical vapor deposition of high-quality single-crystal graphene directly on various dielectric substrates, Adv. Mater. 26 (9) (2014) 1348–1353.
[12] Y.S. Kim, K. Joo, S.K. Jerng, J.H. Lee, E. Yoon, S.H. Chun, Direct growth of patterned graphene on SiO_2 substrates without the use of catalysts or lithography, Nanoscale 6 (17) (2014) 10100–10105.
[13] Q. Liu, Y. Gong, T. Wang, W.L. Chan, J. Wu, Metal-catalyst-free and controllable growth of high-quality monolayer and AB-stacked bilayer graphene on silicon dioxide, Carbon 96 (2016) 203–211.
[14] H.J. Song, M. Son, C. Park, H. Lim, M.P. Levendorf, A.W. Tsen, et al., Large scale metal-free synthesis of graphene on sapphire and transfer-free device fabrication, Nanoscale 4 (10) (2012) 3050–3054.
[15] J. Hwang, M. Kim, D. Campbell, H.A. Alsalman, J.Y. Kwak, S. Shivaraman, et al., van der Waals epitaxial growth of graphene on sapphire by chemical vapor deposition without a metal catalyst, ACS Nano 7 (1) (2013) 385–395.
[16] J. Sun, Y. Chen, M.K. Priydarshi, Z. Chen, A. Bachmatiuk, Z. Zou, et al., Direct chemical vapor deposition-derived graphene glasses targeting wide ranged applications, Nano Lett. 15 (9) (2015) 5846–5854.
[17] J. Sun, Y. Chen, X. Cai, B. Ma, Z. Chen, M.K. Priydarshi, et al., Direct low-temperature synthesis of graphene on various glasses by plasma-enhanced chemical vapor deposition for versatile, cost-effective electrodes, Nano Res. 8 (11) (2015) 3496–3504.
[18] Y. Chen, J. Sun, J. Gao, F. Du, Q. Han, Y. Nie, et al., Growing uniform graphene disks and films on molten glass for heating devices and cell culture, Adv. Mater. 27 (47) (2015) 7839–7846.
[19] S.M. Huang, Q.R. Cai, J.Y. Chen, Y. Qian, L.J. Zhang, Metal-catalyst-free growth of single-walled carbon nanotubes on substrates, J. Am. Chem. Soc. 131 (6) (2009) 2094–2095.
[20] B.L. Liu, W.C. Ren, L.B. Gao, S.S. Li, S.F. Pei, C. Liu, et al., Metal-catalyst-free growth of single-walled carbon nanotubes, J. Am. Chem. Soc. 131 (6) (2009) 2082–2083.
[21] B.L. Liu, D.M. Tang, C.H. Sun, C. Liu, W.C. Ren, F. Li, et al., Importance of oxygen in the metal-free catalytic growth of single-walled carbon nanotubes from SiO_x by a vapor-solid-solid mechanism, J. Am. Chem. Soc. 133 (2) (2011) 197–199.
[22] L. Kang, Y. Hu, L. Liu, J. Wu, S. Zhang, Q. Zhao, et al., Growth of close-packed semiconducting single-walled carbon nanotube arrays using oxygen-deficient TiO_2 nanoparticles as catalysts, Nano Lett. 15 (1) (2015) 403–409.
[23] W.J. Ong, M.M. Gui, S.P. Chai, A.R. Mohamed, Direct growth of carbon nanotubes on Ni/TiO_2 as next generation catalysts for photoreduction of CO_2 to methane by water under visible light irradiation, RSC Adv. 3 (14) (2013) 4505–4509.
[24] W. Menesklou, H.J. Schreiner, K.H. Hardtl, E. Ivers-Tiffee, High temperature oxygen sensors based on doped $SrTiO_3$, Sens. Actuat B Chem. 59 (2–3) (1999) 184–189.
[25] J.C. Ruiz-Morales, J. Canales-Vazquez, C. Savaniu, D. Marrero-Lopez, W.Z. Zhou, J.T.S. Irvine, Disruption of extended defects in solid oxide fuel cell anodes for methane oxidation, Nature 439 (7076) (2006) 568–571.
[26] J. Im, O. Auciello, S.K. Streiffer, Layered barium strontium titanate thin films for high frequency tunable devices, Thin Solid Films 413 (1–2) (2002) 243–247.
[27] J. Sun, A.A. Koos, F. Dillon, K. Jurkschat, M.R. Castell, N. Grobert, Synthesis of carbon nanocoil forests on $BaSrTiO_3$ substrates with the aid of a Sn catalyst, Carbon 60 (2013) 5–15.
[28] J. Sun, C. Wu, F. Silly, A.A. Koos, F. Dillon, N. Grobert, et al., Controlled growth of Ni nanocrystals on $SrTiO_3$ and their application in the catalytic synthesis of carbon nanotubes, Chem. Commun. 49 (36) (2013) 3748–3750.
[29] J. Sun, T. Gao, X. Song, Y. Zhao, Y. Lin, H. Wang, et al., Direct growth of high-quality graphene on high-κ dielectric $SrTiO_3$ substrates, J. Am. Chem. Soc. 136 (18) (2014) 6574–6577.
[30] M.R. Castell, Nanostructures on the $SrTiO_3$ (001) surface studied by STM, Surf. Sci. 516 (1–2) (2002) 33–42.
[31] M.R. Castell, Scanning tunneling microscopy of reconstructions on the $SrTiO_3$ (001) surface, Surf. Sci. 505 (2002) 1–13.
[32] F. Silly, M.R. Castell, Selecting the shape of supported metal nanocrystals: Pd huts, hexagons, or pyramids on $SrTiO_3$ (001), Phys. Rev. Lett. 94 (4) (2005) 046103.
[33] D.S. Deak, F. Silly, D.T. Newell, M.R. Castell, Ordering of TiO_2-based nanostructures on $SrTiO_3$ (001) surfaces, J. Phys. Chem. B 110 (18) (2006) 9246–9251.
[34] M.S.J. Marshall, A.E. Becerra-Toledo, L.D. Marks, M.R. Castell, Surface and defect structure of oxide nanowires on $SrTiO_3$, Phys. Rev. Lett. 107 (8) (2011) 086102.
[35] M.S.J. Marshall, A.E. Becerra-Toledo, D.J. Payne, R.G. Egdell, L.D. Marks, M.R. Castell, Structure and composition of linear TiO_x nanostructures on $SrTiO_3$ (001), Phys. Rev. B 86 (12) (2012) 125416.
[36] A.E. Becerra-Toledo, M.S.J. Marshall, M.R. Castell, L.D. Marks, c(4×2) and related structural units on the $SrTiO_3$ (001) surface: Scanning tunneling microscopy, density functional theory, and atomic structure, J. Chem. Phys. 136 (21) (2012) 214701.
[37] A.E. Becerra-Toledo, M.R. Castell, L.D. Marks, Water adsorption on $SrTiO_3$ (001): I. Experimental and simulated STM, Surf. Sci. 606 (7–8) (2012) 762–765.
[38] D.T. Newell, A. Harrison, F. Silly, M.R. Castell, $SrTiO_3$ (001)-(sqrt5 × sqrt5)-R26.6° reconstruction: a surface resulting from phase separation in a reducing environment, Phys. Rev. B 75 (20) (2007) 205429.
[39] M. Kawasaki, K. Takahashi, T. Maeda, R. Tsuchiya, M. Shinohara, O. Ishiyama, et al., Atomic control of the $SrTiO_3$ crystal surface, Science 266 (5190) (1994) 1540–1542.
[40] N. Grobert, Novel Carbon Nanostructures, University of Sussex, 2000. PhD thesis.
[41] A.T. Murdock, A.A. Koos, T.B. Britton, L. Houben, T. Batten, T. Zhang, et al., Controlling the orientation, edge geometry, and thickness of chemical vapor deposition graphene, ACS Nano 7 (2) (2013) 1351–1359.
[42] A.C. Ferrari, Raman spectroscopy of graphene and graphite: disorder, electron-phonon coupling, doping and nonadiabatic effects, Solid State Commun. 143 (1–2) (2007) 47–57.

[43] A.C. Ferrari, J.C. Meyer, V. Scardaci, C. Casiraghi, M. Lazzeri, F. Mauri, et al., Raman spectrum of graphene and graphene layers, Phys. Rev. Lett. 97 (18) (2006) 187401.
[44] I.O. Maciel, N. Anderson, M.A. Pimenta, A. Hartschuh, H. Qian, M. Terrones, et al., Electron and phonon renormalization near charged defects in carbon nanotubes, Nat. Mater. 7 (11) (2008) 878–883.
[45] D. Takagi, Y. Kobayashi, Y. Homma, Carbon nanotube growth from diamond, J. Am. Chem. Soc. 131 (20) (2009) 6922–6923.
[46] Z.Y. Zeng, J.H. Lin, Metal-catalyst-free growth of carbon nanotubes/carbon nanofibers on carbon blacks using chemical vapor deposition, RSC Adv. 4 (76) (2014) 40251–40258.
[47] J.K. Seo, H. Jung, J.H. Lee, S.Y. Deok, J.J. Young, W.S. Choi, Metal-free CNTs grown on glass substrate by microwave PECVD, Curr. Appl. Phys. 10 (3) (2010) S447–S450.
[48] J.H. Lin, C.S. Chen, M.H. Rümmeli, A. Bachmatiuk, Z.Y. Zeng, H.L. Ma, et al., Growth of carbon nanotubes catalyzed by defect-rich graphite surfaces, Chem. Mater. 23 (7) (2011) 1637–1639.